Solar Physics (2006) 238: 117–139
DOI: 10.1007/s11207-006-0167-5

USING THE EVOLUTION OF CORONAL DIMMING REGIONS TO PROBE THE GLOBAL MAGNETIC FIELD TOPOLOGY

"UNIDENTICAL TWINS": A NEW INTERPRETATION OF THE 12 MAY 1997 EVENT

G. ATTRILL
University College London, Mullard Space Science Laboratory, Holmbury St. Mary, Dorking, Surrey, RH5 6NT, U.K.
(e-mail: gdra@mssl.ucl.ac.uk)

M.S. NAKWACKI
Instituto de Astronomía y Física del Espacio, CONICET-UBA, CC. 67, Suc. 28, 1428 Buenos Aires, Argentina

L.K. HARRA
University College London, Mullard Space Science Laboratory, Holmbury St. Mary, Dorking, Surrey, RH5 6NT, U.K.

L. VAN DRIEL-GESZTELYI
University College London, Mullard Space Science Laboratory, Holmbury St. Mary, Dorking, Surrey, RH5 6NT, U.K.; Observatoire de Paris, LESIA, FRE 2461 (CNRS), F-92195 Meudon Principal Cedex, France; Konkoly Observatory of the Hungarian Academy of Sciences, Budapest, Hungary

C.H. MANDRINI
Instituto de Astronomía y Física del Espacio, CONICET-UBA, CC. 67, Suc. 28, 1428 Buenos Aires, Argentina

S. DASSO
Instituto de Astronomía y Física del Espacio, CONICET-UBA, CC. 67, Suc. 28, 1428 Buenos Aires, Argentina; Departamento de Física, Facultad de Ciencias Exactas y Naturales, Universidad de Buenos Aires, 1428 Buenos Aires, Argentina

and

J. WANG
National Astronomical Observatory, Chinese Academy of Sciences, Beijing, China

(Received 6 March 2006; accepted 10 July 2006; Published online 27 August 2006)

Abstract. We demonstrate that study of the evolving magnetic nature of coronal dimming regions can be used to probe the large-scale magnetic structure involved in the eruption of a coronal mass ejection (CME). We analyse the intensity evolution of coronal dimming regions using 195 Å data from the Extreme ultraviolet Imaging Telescope (EIT) on board the Solar and Heliospheric Observatory (SOHO). We measure the magnetic flux, using data from the SOHO/Michelson Doppler Imager (MDI), in the regions that seem most likely to be related to plasma removal. Then, we compare these magnetic flux measurements to the flux in the associated magnetic cloud (MC). Here, we present our analysis of the well-studied event on 12 May 1997 that took place just after solar minimum in

a simple magnetic configuration. We present a synthesis of results already published and propose that driven "interchange reconnection" between the expanding CME structure with "open" field lines of the northern coronal hole region led to the asymmetric temporal and spatial evolution of the two main dimming regions, associated with this event. As a result of this reconnection process, we find the southern-most dimming region to be the principal foot-point of the MC. The magnetic flux from this dimming region and that of the MC are found to be in close agreement within the same order of magnitude, 10^{21} Mx.

1. Introduction

1.1. Coronal dimmings

One particular feature that has been observed when a coronal mass ejection (CME) occurs is a phenomenon known as coronal dimming. A dimming can be observed as an intensity decrease in images of the solar atmosphere and can appear relatively suddenly (in tens of minutes). Dimmings were first observed at optical wavelengths in ground-based coronagraph data (Hansen *et al.*, 1974), with the first space-based observation being made in soft X-rays by the Skylab mission (1973 – 1974). These dimmings were referred to as "transient coronal holes" (TCHs) (Rust, 1983). Since these first early observations, dimmings have also been observed in *Yohkoh* soft X-ray telescope (SXT) data (e.g. Sterling and Hudson, 1997) and in SOHO/Extreme Ultra-Violet Imaging Telescope (EIT) 195 Å data (e.g. Thompson *et al.*, 1998).

The cause of these dimmings has been much debated in the literature. At present, there appear to be two generally accepted possibilities. Firstly, the dimming may be due to a density depletion caused by an evacuation of plasma (Hudson, Acton, and Freeland, 1996). Such an effect may be caused by the eruption of the local magnetic field, leading to considerable expansion of magnetic loops into interplanetary space. Following eruption, a region of decreased plasma density is left behind. Supporting this interpretation is the study of plasma Doppler motions using SOHO/CDS (Coronal Diagnostic Spectrometer) data by Harra and Sterling (2001). They found strong, direct evidence of blue-shifted mass motion in coronal dimming regions, concluding that the dimming is indeed due to plasma evacuation. Harrison and Lyons (2000) came to a similar conclusion based on work that focused on density depletion in coronal dimming regions, emphasising that the dimming is mainly caused by a loss of plasma at a temperature of 1×10^6 K. Work by Zarro *et al.* (1999), compared *Yohkoh* SXT and EIT observations, establishing that similar co-spatial dimmings exist simultaneously at different wavelengths, thus strengthening the theory that the dimmings could indeed be caused by a decrease in coronal density. Recently, ground-based observations of TCHs have also been made in the He I 1083 nm line (de Toma *et al.*, 2005). In this line, the brightenings are co-spatial and co-temporal with EUV dimmings and are believed to be induced by a decrease of the overlying coronal radiation. The brightenings are therefore interpreted as manifestations of the decreased coronal density caused by the ejection of coronal material.

Other works (Thompson *et al.*, 1998; Chertok and Grechnev, 2003) have highlighted another possible cause of the dimmings. Differences observed between images in different emission lines suggest that some secondary temperature variations may also be responsible for the appearance of dimmings. However, it has been noted that the dimmings appear on timescales that are shorter than those of radiative cooling in the corona (Thompson *et al.*, 1998), suggesting that the dimmings are mainly a result of density depletion rather than a temperature effect.

1.2. The link with CMEs

Coronal dimmings have been acknowledged as a reliable indicator of front-side CMEs (Thompson *et al.*, 2000). "Double dimmings" can appear in the concavities of sigmoidal-type structures, such as the dimmings on the 7 April 1997 (Sterling and Hudson, 1997). Another classical "double dimming" took place on 12 May 1997 (Thompson *et al.*, 1998), and it was suggested that the dimmings mark the position of flux rope foot-points (Webb *et al.*, 2000). Upon eruption of the flux rope (which makes up the core field of the associated CME), the magnetic loops rooted in the dimming regions "open" to the solar wind. The regions become dark as plasma expands or escapes along the "open" field lines (Thompson *et al.*, 2000). Other authors contest the interpretation that TCHs may be the sole source regions of magnetic clouds (e.g. Kahler and Hudson, 2001).

Strengthening the link between coronal dimming regions and CMEs are studies of mass (e.g. Sterling and Hudson, 1997; Wang *et al.*, 2002; Zhukov and Auchère, 2004). Although large uncertainties are associated with estimates of coronal mass loss (due to the dependence of calculations on the emission measure distribution, which is not well known, and uncertainties in estimating the volume of the dimming regions), the results do suggest that at least part of the CME mass comes from coronal dimming regions. Indeed, Harrison and Lyons (2000) conclude that the mass evacuated from the dimming regions may account for much of the mass of the outer shell of the CME. For the 12 May 1997 event, Zhukov and Auchère (2004) calculate that 50% of the mass of the CME comes from TCHs, and the other 50% from a more extended region. Dimmings observed in the low corona in extreme ultraviolet (EUV) and X-rays generally develop approximately 30 minutes before the appearance of a CME in SOHO/Large Angle and Spectrometric Coronagraph (LASCO) data (Thompson *et al.*, 2000). The spatial correspondence between coronal dimming regions observed in EUV and the angular extent of the associated CME further supports this link (Thompson *et al.*, 2000).

Given the close relationship between the manifestation of coronal dimming regions and CMEs, the drive to understand the magnetic nature of CMEs naturally requires investigation of the magnetic nature of dimming regions.

This paper focuses on the extensively reviewed eruption on 12 May 1997. We re-visit this well-studied event, as it is an excellent case with which to present our method of analysis. In the following section, we present a synthesis of already published results.

1.3. The event of 12 May 1997

The event occurred just after solar minimum, hence the magnetic structure of the Sun was relatively simple. The eruption originated in active region (AR) 8038 (N21W09) and was associated with a (long duration) GOES class C1.3 flare, starting at 04:42 UT and reaching its peak around 04:55 UT (Thompson *et al.*, 1998). AR8038 was an isolated AR and the result of new flux emergence during Carrington rotation 1922.

A strong coronal wave signature with a velocity of $245 \pm 40\,\mathrm{km\,s^{-1}}$ was associated with the eruption, and it has been noted that the appearance of the coronal wave coincided with the appearance of the coronal dimming regions (Thompson *et al.*, 1998). The coronal wave propagated fairly isotropically, emanating from or near AR8038, exhibiting deceleration as it approached the north polar coronal hole (Thompson *et al.*, 1998).

A long emitting chain, visible as a conspicuous brightening, gradually encompassed the entire coronal hole boundary remaining visible for several hours (Chertok and Grechnev, 2003). Such a feature has also been observed in other events (e.g. 13 November 1994) and referred to as "Aurora Solaris" (Hudson, Acton, and Freeland, 1996). Sterling and Moore (2001) reported a similar phenomenon which they termed "EIT crinkles".

There was also a filament eruption associated with this event. Webb *et al.* (2000) provided Hα data (see their Figure 2) showing the eruption to commence sometime between 04:43 and 04:47 UT. The LASCO/CME catalogue records a full halo CME associated with this eruption.

Figure 1 shows an EIT 195 Å image. The two main dimming regions can easily be identified, located slightly to the north of the centre of the solar equator. This image shows that the dimming regions appear to have an intensity similar to the north and south polar coronal holes, hence the term "transient coronal holes".

Webb *et al.* (2000) provided a detailed analysis of this event. They measured the magnetic flux in the dimming regions, finding the north-east dimming to have a dominant negative polarity and the south-west dimming to have a dominant positive polarity. They suggested that the dual dimming regions that are joined to the flare loops may be the foot-points of a magnetic flux rope structure that erupts forming the core of the CME.

In the same paper, Webb *et al.* (2000) analysed the interplanetary events linked to the solar eruption. An interplanetary shock was observed arriving at the Wind spacecraft on 15 May at 01:15 UT, and a magnetic cloud (MC) followed the shock

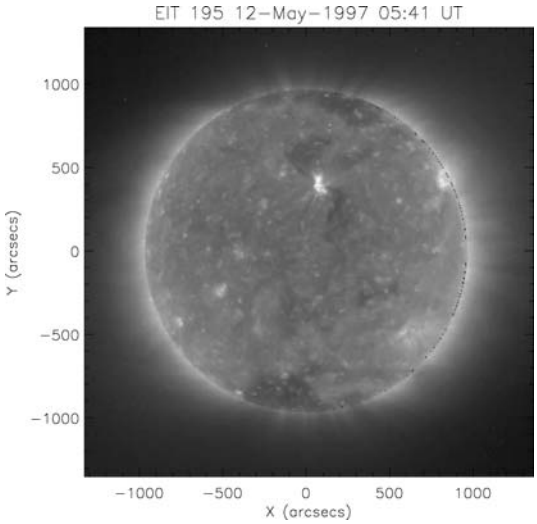

Figure 1. EIT 195 Å image showing the existing polar coronal holes and the two main dimming regions at 05:41 UT on 12 May 1997. The main dimmings appear to be attached to the bright flare loops.

at ≈10:00 UT on the same day. The authors modelled the interplanetary flux rope and computed its physical parameters, which they compared to the corresponding coronal ones. The southward magnetic field associated with these structures lasted long enough to trigger a geomagnetic storm on Earth.

In this paper, we combine SOHO/EIT (Delaboudiniére *et al.*, 1995) 195 Å data and SOHO/Michelson Doppler Imager (MDI; Scherrer *et al.*, 1995) magnetic maps to build up a picture of the evolution of the dimming regions. We also use *Yohkoh* SXT (Tsuneta *et al.*, 1991) observations to study the global aspects of the event. We model the MC using *in situ* data from the Magnetic Field Investigation (MFI; Lepping *et al.*, 1995) aboard Wind, and compare its magnetic flux with that measured within the dimming regions. From our analysis of the asymmetric evolution of the unidentical twin dimming regions, we derive a new scenario that explains both the global observations of this event and the magnetic flux measurements in the associated MC.

2. Solar Data Analysis and Results

2.1. Processing EIT data

SOHO/EIT 195 Å full-disk images, at approximately 17 min intervals with a pixel size of 5.26″, are used in our study. The 195 Å bandpass is dominated by Fe XII emission lines at 192.3, 193.5 and 195.1 Å, corresponding to a temperature of

$\approx 1.5 \times 10^6$ K at typical coronal densities. All EIT heliograms are differentially de-rotated to the same pre-event time (00:12 UT). To visualise the dimmings clearly, we produce base difference images where the same pre-event image is subtracted from all subsequent images. We use base difference images (as opposed to running difference images) because false dimmings (due to a change in intensity of a bright structure or displacement of a feature between successive frames) can be created when using the running difference method (Chertok *et al.*, 2004; Chertok and Grechnev, 2005).

Our data set runs from 00:00 UT on 12 May 1997 until ≈00:00 UT on 14 May 1997 before limb brightening/darkening effects, due to the de-rotation, encroach on disk centre where the main dimming regions are located.

2.2. Defining the boundary of the dimmings

In order to carefully analyse the dimming regions, we need to impose a quantifiable boundary. We consider that a TCH may be defined as a region that exhibits an intensity decrease to more like that of a coronal hole. Considering this, we employ a contour method with the contour level set to lie halfway between the intensity of an area of the quiet Sun and that of an existing coronal hole.

Figure 2 shows the main dimming regions and the application of our criterion to define the boundaries. It is encouraging to note that at the maximum spatial extent of the dimmings, our contour method highlights a region which is very similar to that corresponding to the "full size of the dimmings", automatically defined

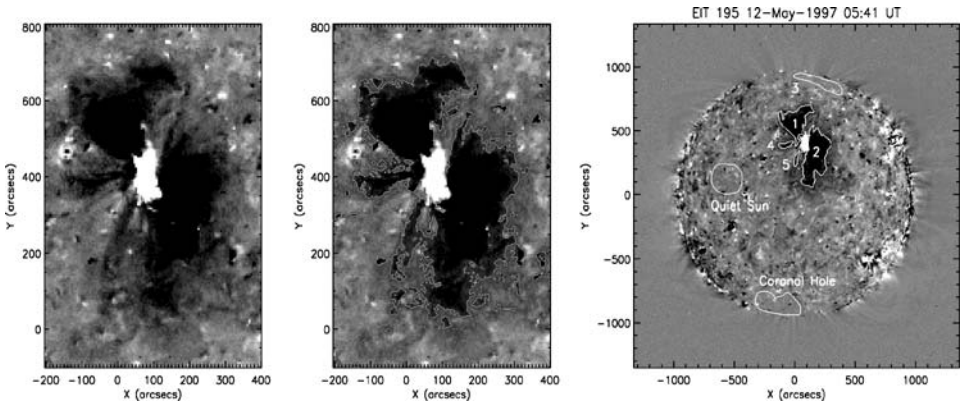

Figure 2. Left panel: Base difference image (05:41 – 00:12 UT) at the maximum spatial extent of the dimmings, showing the main dimming area. *Centre panel* shows the dimming regions defined by our contour boundary method. *Right panel* shows the regions selected for analysis. *Regions* 1 and 2 are the main dimming regions. *Regions* 4 and 5 are smaller dimming regions identified by the contour method. *Region* 3 is situated in the north polar coronal hole. Also shown are the (relatively undisturbed) quiet Sun and south polar coronal hole regions, used for comparison purposes in this study.

by the region-growing method of Podladchikova and Berghmans (2005) (see their Figure 3d). Having defined the boundaries of the dimmings, we are able to select separate regions for analysis. Figure 2 (right panel) shows the selected regions.

2.3. TEMPORAL INTENSITY EVOLUTION OF THE DIMMINGS

We compute light curves (see Figure 3) from the EIT images in the selected regions to measure quantitatively the variation of emission in time. The light curves are made for each region independently by averaging the EUV emission over the corresponding area (see Figure 2). In addition, we examine the south polar coronal hole, as well as a (relatively undisturbed) quiet-Sun region of the solar disk. The corresponding light curves are shown for comparison at the base of each plot with thin solid and thin dashed lines, respectively.

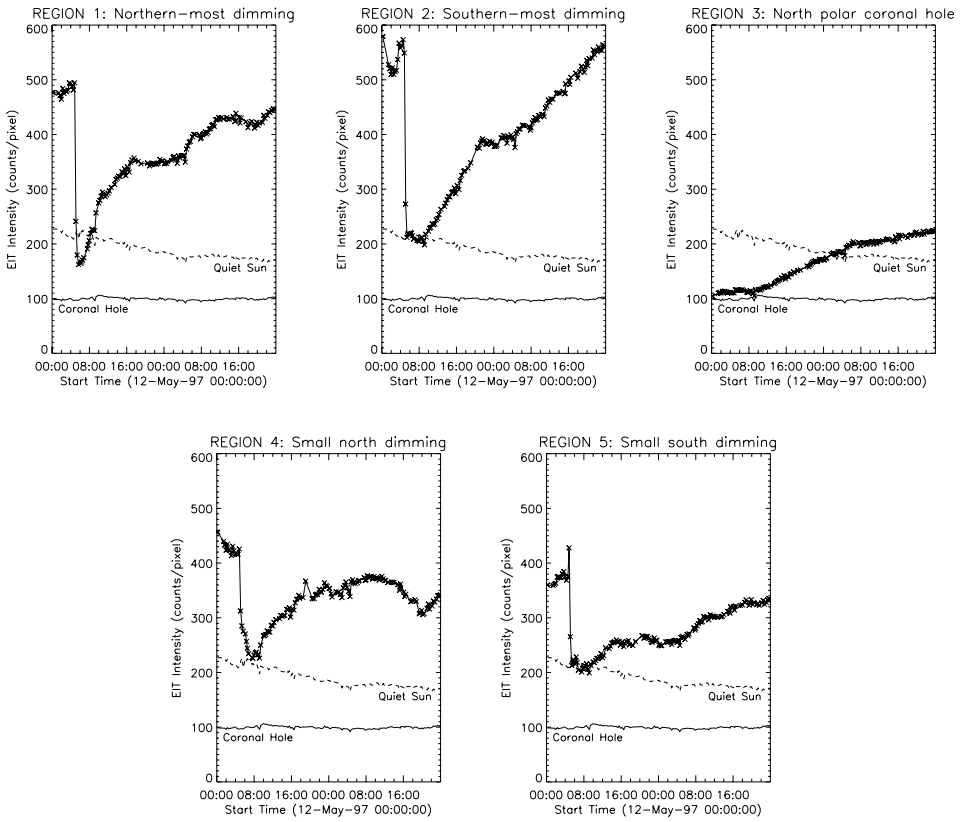

Figure 3. Light curves showing the temporal variation in EUV intensity averaged over the selected region (counts/pixel). The light curves are made from the static regions of interest shown in Figure 2. The *thin solid* and *thin dashed* light curves at the base of each plot show the intensity variation in the (relatively undisturbed) south polar coronal hole and quiet Sun, respectively.

TABLE I
Time of onset and of maximum dimming for each region.

Region	Dimming onset (UT)	Dimming maximum (UT)
1 (Main N dimming)	04:50	05:41
2 (Main S dimming)	04:34	09:10
4 (Small N dimming)	04:50	07:45
5 (Small S dimming)	04:50	09:10

The intensity in the two main dimmings (regions 1 and 2) drops significantly at 04:50 and 04:34 UT, respectively. Region 3 (the north polar coronal hole) shows a significant gradual brightening to approximately the quiet Sun intensity level. Table I shows the time of the dimming onset and the time of the maximum dimming for each region, as inferred from the light curves.

The light curves can be used as a tool to visualise the physical restructuring of the magnetic field topology. The sharp drop in intensity seen in the light curves is consistent with the process of plasma evacuation, caused by the rapid expansion or "opening" of the magnetic field during the initial phase of the eruption. We interpret the point where the intensity starts to recover as the magnetic field experiencing a change in its physical condition, from an "open" towards a "closed" state that allows the re-accumulation of plasma, producing the observed recovery in intensity.

Our results show that the time of the maximum dimming occurs in region 1 at 05:41 UT and in region 2 at 09:10 UT (see Table I). Prior to this study, the dimming regions have been considered only as one unit, "twin" dimmings, rather than as separate entities (e.g. Thompson *et al.* (1998) state that the strongest decrease in emission measure occurs near 06:22 UT).

The recovering intensity of the dimmed regions appears to be a relatively steady, gradual process, although the light curves do show some variation. The sharp gradient visible in the light curve of region 1, immediately after the point of maximum dimming, is most probably due to the expansion and brightening of the flare loops that appear to link the two main dimming regions. The bright flare loops seem to affect region 1 more than region 2 because of line-of-sight projection effects.

The time at which the dimmings appear suggests that the magnetic field rooted in region 2 has expanded first (either driven by the erupting filament disturbance or creating the conditions for the eruption to occur). In either case, the disturbance starts in the south, proceeding northward. The onset of the dimming of region 1 occurs at $\approx$ 04:50 UT, we associate this with the time at which the disturbance reaches that location.

2.4. Evolving dimmings

As noted by Kahler and Hudson (2001), the boundaries of TCHs are constantly evolving. To study the evolution of the dimming boundaries, we examine contours

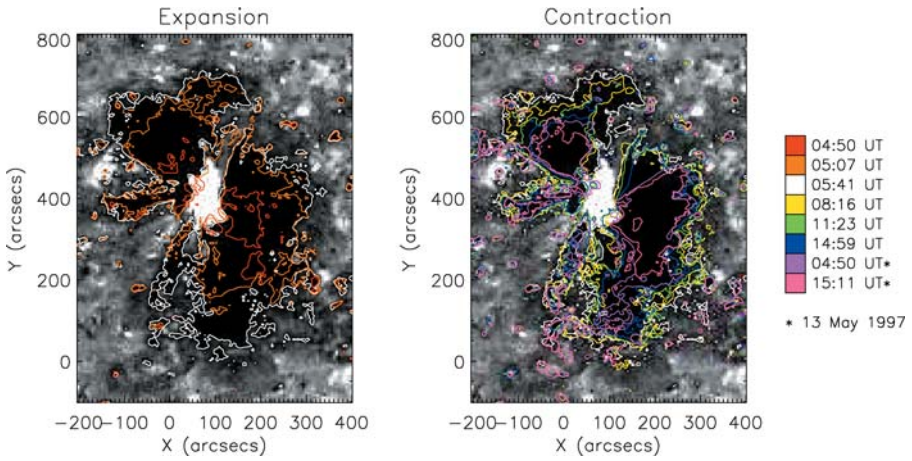

Figure 4. Asymmetric temporal and spatial evolution of the unidentical twin dimmings. The image on the *left* shows the expansion of the dimming regions. The image on the *right* shows the contraction of the dimming region boundaries. The colour bar on the right shows the times of the coloured contours. The contours are overlaid on a background showing the base difference image at 05:41 UT.

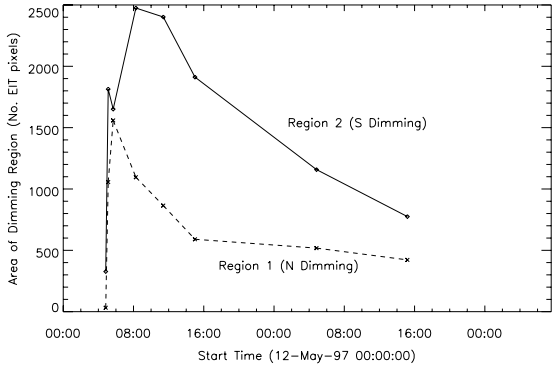

Figure 5. Evolution of the area of the two main dimming regions. The *dashed line* shows the change in area of region 1 and the *solid line* shows the change in area of region 2. The graph clearly shows the rapid expansion of the dimming regions and the relatively gradual contraction.

from images at successive intervals throughout our data set. Figure 4 shows the expansion and subsequent contraction of the dimming regions.

The expansion of the dimming regions happens very fast, too quickly for the cadence of EIT to capture in much detail. In contrast, the contraction or recovery is more gradual, allowing us to examine the evolution. We can actually see the shrinking of the dimming regions in an EIT 195 Å movie. Figure 5 shows the change in area of the two main dimming regions, as a function of time. It is clear from Figures 4 and 5 that the twin dimming regions are unidentical. They exhibit an asymmetric temporal and spatial evolution, particularly evident in the recovery

phase. Region 1 (the north-east dimming region) starts to contract before region 2 (the south-west dimming region).

2.5. Processing MDI data

SOHO/MDI level 1.8 full-disk magnetograms with a 96 min cadence and a pixel size of 1.98″ were used in this study. The data were corrected for radial projection effects using the standard `zradialize` routine. Since previous studies (e.g. Berger and Lites, 2003; Wang *et al.*, 2003) have shown that MDI significantly underestimates the magnetic flux, we have corrected both the linear and non-linear response of MDI using the expression $\phi_{\text{corrected}} = 1.45(\phi + 0.3\phi_{>1200\text{G}})$, as indicated in Green *et al.* (2003).

After correcting for underestimation, we proceed to measure the magnetic flux within the dimming regions, which extend from the AR main polarities to the quiet Sun. Therefore, the magnetic flux associated with the dimmings has two components: an AR and a quiet-Sun region part. To accurately calculate the magnetic flux in each dimming region, we follow the method described in Section 3.2 of Mandrini *et al.* (2005). Part of the flux in the dimmings in the quiet-Sun regions is due to noise and part forms small-scale connectivities. Such flux does not contribute to the overall net flux of the dimmings. To avoid incorporating this flux into our calculations, we first removed the AR flux from each dimming region and filtered the flux in the quiet-Sun part of the dimmings using a threshold of 20 G. After filtering, we then added the AR flux to obtain the total magnetic flux in each dimming region. So the magnetic flux measurement is the sum of both the AR *and* the filtered quiet-Sun magnetic flux components.

2.6. Magnetic flux at the maximum extent of the dimmings

The MDI image shown in Figure 6 is used to measure the magnetic flux within the EIT dimming region boundaries shown (the same as in Figure 2). The only concentrated AR on the visible disk is AR8038, consisting of a somewhat dispersed negative polarity and a compact positive polarity. The north pole is dominantly positive, while the south pole is dominantly negative, consistent with the global configuration for 1997, during the first part of solar cycle 23.

Table II shows the measurements of the magnetic flux through each dimming region. We measure the magnetic flux within regions 1, 2, 4 and 5. We do not measure the magnetic flux within region 3 because it is located in the north polar coronal hole, where the magnetogram suffers from serious projection effects (Hagenaar, Schrijver, and Title, 2003). We measure the total positive and total negative magnetic flux in each dimming region; then, we calculate the absolute flux as the sum of the magnitude of both the positive and negative fluxes. Finally, we compute the net flux by subtracting them. Since the majority of small-scale mixed polarities close in their direct vicinity, the net flux provides an estimate of how much flux is potentially

TABLE II

Magnetic flux measurements in the dimming regions at their maximum spatial extent (see Figures 2 and 6).

Region	Positive flux (Mx)	Negative flux (Mx)	Absolute flux (Mx)	Net flux (Mx)
1	2×10^{20}	-11×10^{20}	13×10^{20}	-9×10^{20}
2	24×10^{20}	-3×10^{20}	27×10^{20}	21×10^{20}
4	0.1×10^{20}	-1×10^{20}	1.1×10^{20}	-0.9×10^{20}
5	0.2×10^{20}	-0.1×10^{20}	0.3×10^{20}	0.1×10^{20}

The total positive (negative) magnetic flux is the sum of all of the positive (negative) flux that lies within the dimming region boundary. The absolute flux is the sum of the magnitude of both positive and negative fluxes, and the net flux is the difference between them.

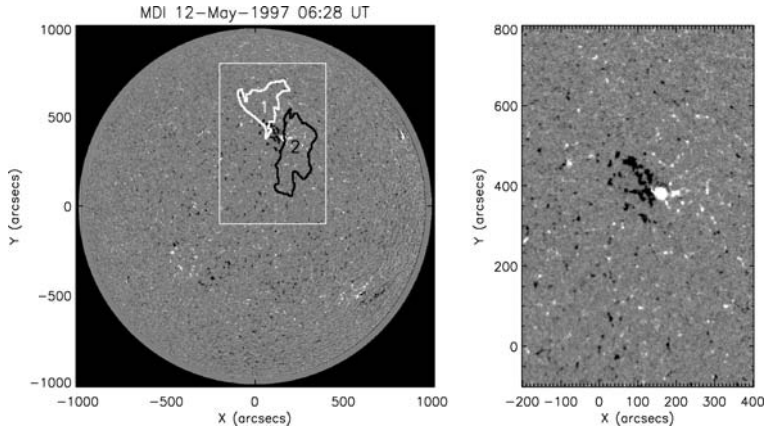

Figure 6. The *left panel* shows the MDI full-disk image at 06:28 UT on 12 May 1997. Overlaid are the locations of the two main dimming regions seen in Figure 2. The *right panel* shows a close-up of the rectangular region defined in the *left panel*. In *white* (*black*), we indicate regions of positive (negative) polarity.

free for connection with magnetic flux outside the selected region. At the maximum extent of the dimming, the net flux in region 1 is found to be -9×10^{20} Mx and the net flux in region 2 is found to be 21×10^{20} Mx (see Table II). The total absolute flux through regions 1, 2, 4 and 5 is 41×10^{20} Mx.

Our measurement of the net flux through region 1 is in agreement with that of Webb *et al.* (2000), but our measurement through region 2 is almost double their result. They found the flux for region 1 to be -9×10^{20} Mx and for region 2 to be 12×10^{20} Mx. The authors note that their measurement for region 2 is less precise due to the presence of the positive polarity sunspot. The same uncertainty remains in our measurement, since the magnitude of the measured magnetic flux depends strongly on the extent of involvement of this concentrated magnetic field. Since the dimming boundaries can be determined with a precision of ± 2 EIT pixels (after

Mandrini *et al.*, 2005), we measure how much the magnetic flux changes when we purposely shift the dimming region boundary by 2 EIT pixels in all four cardinal directions. We measure a maximum difference of $\pm 7 \times 10^{20}$ Mx, obtained when moving the boundary east – west due to the extent to which the sunspot is included in the measurement. We take this maximum measured error as the uncertainty in our measured solar flux measurements. If the interpretation of Webb *et al.* (2000), is correct, so that the main dimming regions (1 and 2) do indeed mark the foot-points of the magnetic flux rope that erupts as the core of the CME, then our calculation of the total absolute flux should be halved to account for the fact that we are measuring the flux through both foot-points. This yields a total "linked" flux of $(21 \pm 7) \times 10^{20}$ Mx and is substantially larger than the total "linked" flux result $(10 \pm 2) \times 10^{20}$ Mx of Webb *et al.* (2000). There are probably three main reasons for this. Firstly, the regions through which the magnetic flux is calculated are substantially larger in our study than in Webb's (compare their Figure 3 and our Figure 6), although the larger extent of our regions just increases the quiet-Sun magnetic flux content, so this probably only accounts for a small proportion of the larger value. Secondly, we have shown that the measured flux through dimming region 2 depends substantially on the extent of involvement of the sunspot. Thirdly, we have corrected MDI measurements for the recently found underestimation and projection effects, which yields substantially larger magnitudes for the estimated flux contained in the dimming regions. The latter two factors most likely explain our larger values.

2.7. Global nature of the event

In order to build a complete picture of the evolving global magnetic topology of the eruption, we also examine more far-flung effects, such as the brightening at the boundary of the north polar coronal hole (described in Section 1.3). This is visible in both EIT 195 Å and SXT, Figures 7 and 8, respectively. Figure 7 shows

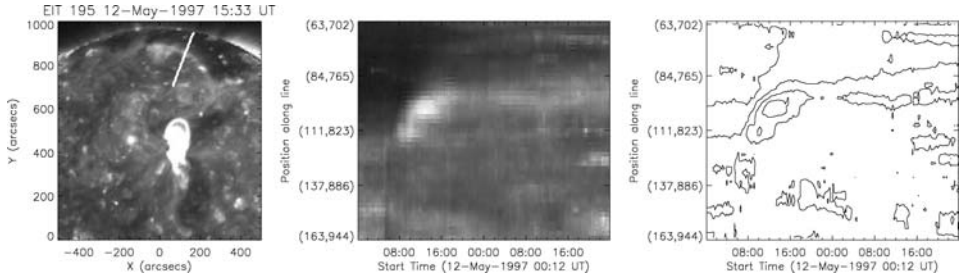

Figure 7. The 2-D intensity profile made along the *thick white line* shown in the *left panel* of this figure. The *centre panel* shows the intensity change along the selected line profile with time. The *right panel* is a contour plot of the intensity profile. The brightening (commencing between 06:49 and 07:35 UT) along the shrinking boundary of the north polar coronal hole is clearly visible.

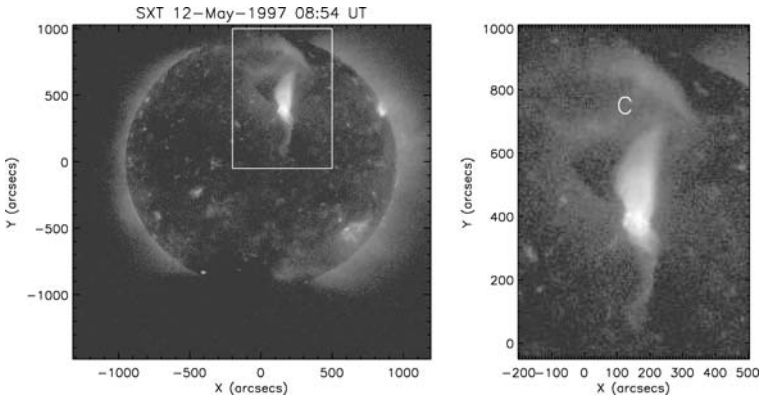

Figure 8. Yohkoh SXT image at 08:54 UT on 12 May 1997 made using the thin aluminium filter. The two main dimming regions can be seen, as well as the cusp-shape over the flare loops. A zoom of the rectangular area defined in the *left panel* is shown in the *right panel*. "**C**" marks the location of hot loops connecting the northern edge of dimming region 1 to the boundary of the north polar coronal hole.

a 2-D intensity profile made across the boundary of the north polar coronal hole. The centre and right panels show the retreating boundary and the brightening. The brightening takes place in two bursts. Co-temporal with the coronal wave associated with this event and with the dimming of region 1, a brief gentle brightening along the north polar coronal hole boundary (from 245 to 275 counts/pixel) occurs between 04:50 and 05:07 UT. A return to pre-disruption conditions takes place by 05:41 UT. Later, between 06:49 and 07:34 UT, a significant brightening is observed at the same location, increasing in intensity steadily, from 245 to a maximum of about 500 counts/pixel between 12:16 and 13:26 UT, before gradually fading to reach a fairly constant condition around 19:00 UT. By this time, the intensity of the pixels has reached a level similar to that of pre-eruption conditions, but the polar coronal hole has shrunk, shifting the boundary considerably farther north.

In addition to the brightening along the north polar coronal hole boundary, the SXT image at 08:54 UT (Figure 8) also shows an extended brightening along the eastern edge of dimming region 2. This brightening may be due to the arcade that presumably formed beneath the main body of the erupted filament (see Section 2.3). This arcade is formed in a weak-field region, which may be why it appears less bright than the flare loop arcade at the heart of AR8038.

3. Interplanetary Data Analysis and Results

3.1. In situ measurements at 1 AU

The flux rope ejected from the Sun on 12 May 1997 was observed by the spacecraft Wind at 1 AU as a left-handed helical structure lying in the ecliptic plane

(Webb *et al.*, 2000). Here, we analyse *in situ* magnetic observations (3 s temporal cadence) obtained by the MFI. The data were downloaded from the public database *http://cdaweb.gsfc.nasa.gov/cdaweb/istp_public/*. In particular, we use the magnetic field vector components measured in the Geocentric Solar Ecliptic (GSE) system, between 10:00 UT on 15 May and 01:00 UT on 16 May, which is the same time period taken by Webb *et al.* (2000). The interplanetary magnetic data in GSE components and other interplanetary observations (such as the bulk wind velocity, electron temperature, etc.) are illustrated in Webb *et al.* (2000), mainly in their Figure 4.

We define a local direction, called $\hat{z}_{\rm cloud}$, that agrees with the direction of the main cloud axis. We apply a Minimum Variance (MV) method (e.g. Sonnerup and Scheible, 1998), which gives a good determination of $\hat{z}_{\rm cloud}$ when the distance between the spacecraft trajectory and the cloud axis (i.e. the impact parameter, p) is small. Webb *et al.* (2000) found that p is 20% of the cloud radius, which justifies the use of the MV method. At the same time, and using the orientation given by MV, we see that the observed magnetic field vector shows a large and coherent rotation (more than 180°, not shown here) in the largest and intermediate variance planes. This is also an indication of a very low impact parameter. We rotate the observed magnetic field components to the cloud local components (as done by Bothmer and Schwenn, 1998; Dasso *et al.*, 2003, 2005). We find that the angle between the cloud axis, which is chosen such that the magnetic field is positive at the cloud centre, and the ecliptic plane (ecliptic latitude) is -2°. Thus, this axis is almost on the ecliptic plane and points slightly to heliospheric south. The angle between the projection of the cloud axis on the ecliptic plane and the Earth – Sun direction is found to be 114° (this projection points to solar east). Thus, the orientation angles determined by us are in good agreement with the ones found by Webb *et al.* (2000). From the obtained MC orientation, the duration of the cloud observations and its velocity, we determine the cloud radius, $R_{\rm MC} = 0.08$ AU.

3.2. Magnetic flux in the magnetic cloud

Webb *et al.* (2000) computed the axial magnetic flux of the interplanetary rope using a single model for its magnetic structure. They compared the computed axial flux to the magnetic flux they determined for the observed dimming regions. In this section, we go a step farther in the interplanetary data analysis to determine more stringent values for the MC physical parameters. We compute the magnetic flux for both components of the cloud field (axial and azimuthal) and we explore different models for the magnetic field structure of the cloud.

We model the local magnetic configuration of the cloud with three different cylindrical and static models. We use Lundquist's model (model **L**, a linear force-free field; Lundquist, 1950), Gold and Hoyle's model (model **G**, a uniformly twisted and non-linear force-free field; Gold and Hoyle, 1960) and Cid's model (model **C**, a

non-force-free model with a constant axial current density and a linear dependence on the radius for the azimuthal component of the current density; Cid *et al.*, 2002). These three models have significantly different helical magnetic configurations with very different distributions of magnetic twist.

We define the three unit vectors of the cylindrical coordinate system, as is usually done, such that $\hat{r}$, $\hat{\varphi}$ and $\hat{z}$ correspond to the radial, azimuthal and axial directions, respectively. Thus, $B_{r,\mathrm{cloud}}$, $B_{\varphi,\mathrm{cloud}}$, and $B_{z,\mathrm{cloud}}$ are the local cloud components of the magnetic field.

We determine the spacecraft distance relative to the magnetic cloud axis, assuming a constant speed for the MC during Wind observations. This distance is null when the spacecraft crosses the cloud axis, so that its radial position is $-R_{\mathrm{MC}}$ when Wind enters the MC and $+R_{\mathrm{MC}}$ when it leaves the cloud.

We first fit the free parameters (magnetic field amplitude and torsion at the cloud axis) of the three models to the full cloud data series, as done in Dasso *et al.* (2003, 2005). We call this first step the symmetric fitting. Then, we split the time series in two parts: (1) the in-bound part (before the spacecraft reaches the magnetic cloud axis) and (2) the out-bound part (after it crosses the axis). In this way, we perform six different fittings, that correspond to three different models in each of these two branches. This allows us to analyse the effect of the in- and out-bound asymmetry, present in the cloud data, on the computed fluxes (see Figure 9).

Figure 9 shows the curves for the different fittings (symmetric **L**, **G** and **C**, in-bound **L**, **G** and **C**, and out-bound **L**, **G** and **C**) and the observations for the two

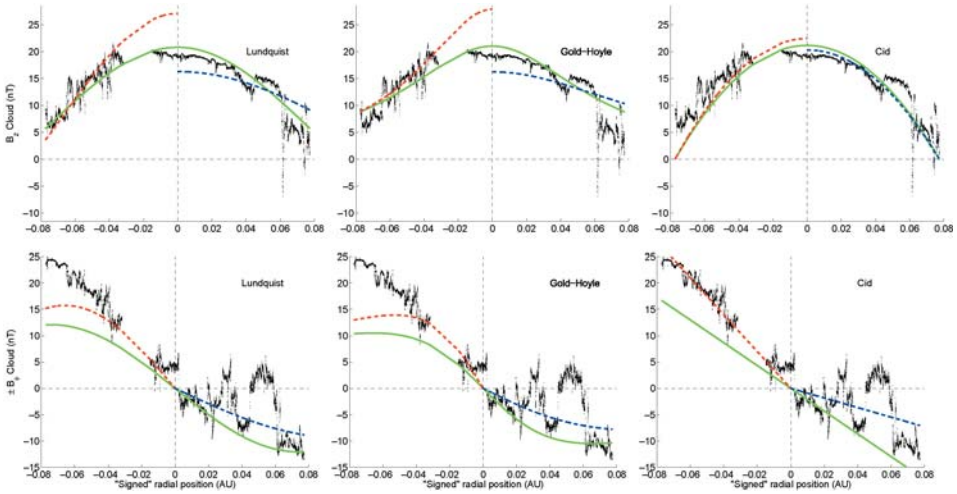

Figure 9. Axial ($B_{z,\mathrm{cloud}}$) and azimuthal ($\pm B_{\varphi,\mathrm{cloud}}$) components of the magnetic field in the cloud (data and fitted curves, see Section 3.2, main text). The *three upper panels* correspond to $B_{z,\mathrm{cloud}}$: models **L** (left), **G** (middle), and **C** (right). Likewise for $\pm B_{\varphi,\mathrm{cloud}}$ in the *lower panel*. *Green full lines* correspond to the symmetric fitting, *dashed red* and *blue lines* to the in-bound and out-bound branches of the asymmetric fitting, respectively.

main components of the cloud magnetic field. The figure is drawn as a function of the radial spacecraft position, as defined earlier. The three upper panels correspond to the $B_{z,\mathrm{cloud}}$ component and the three lower panels to the $\pm B_{\varphi,\mathrm{cloud}}$ component. The negative sign before $B_{\varphi,\mathrm{cloud}}$ (vertical axis in Figure 9) corresponds to $r < 0$ (i.e., the in-bound branch) and the positive to $r > 0$ (i.e., the out-bound branch). The first column in Figure 9 corresponds to model **L**, the second to model **G**, and the third one to model **C**. In each figure, the green continuous line shows the symmetric fitting, the red dashed line the in-bound and the blue dashed line the out-bound fitting for the asymmetric case, respectively. We see that models **L** and **G** behave in a very similar way, but they do not fit the data as well as model **C** does. The data gap that appears near the axis of the cloud is probably responsible for this drawback, this effect can be clearly seen on the asymmetric fittings for $B_{z,\mathrm{cloud}}$ using models **L** and **G**.

The values of χ^2 (defined as the square root of the mean difference between the observed and corresponding modelled components of the magnetic field to the second power for each model), which give a quantitative estimation of the fitting quality, are also affected by the presence of the data gap. For model **C** we obtain the lowest χ^2. The ratio between the maximum (model **G**, symmetric case) and minimum (model **C**, asymmetric in-bound case) χ^2 values is 1.7. If this ratio is equal to 1, it would mean that both fittings have a similar quality; however, in our particular case, model **C** is by far the one that best represents the magnetic structure of the cloud.

From the fitted parameters, we compute the axial (Φ_z) and azimuthal (Φ_φ) magnetic fluxes, which are given by:

$$\Phi_z = 2\pi \int_0^{R_{\mathrm{MC}}} B_z(r) r \, \mathrm{d}r, \quad \Phi_\varphi / L = \int_0^{R_{\mathrm{MC}}} B_\varphi(r) \, \mathrm{d}r \tag{1}$$

where L is the cloud length. Different models (**L**, **G** and **C**) have different expressions for these integrals, we refer the reader to Dasso *et al.* (2006) for details.

Table III shows the obtained values for the axial and azimuthal (per unit length) fluxes. The upper block corresponds to the symmetric fittings and the lower one to the asymmetric ones. The last two rows of each block correspond to the means and the standard deviations of the flux values for symmetric and asymmetric cases, these results (except for the standard deviation in the azimuthal flux) prove to be similar.

Comparing the models, we can see that models **L** and **G** give similar values in all cases, differing from those obtained using model **C**. The range of flux values found for the symmetric fitting is included within the range of fluxes for the asymmetric case. As the cloud observations are asymmetric, but the full data fitting is forced to be symmetric (for the three models), the dispersion in the fitting of the split temporal data are larger. We take as each flux value its mean $\pm$ the dispersion obtained in the asymmetric case, which we consider to be more realistic. Thus, we estimate the fluxes as $\Phi_z \approx (4.8 \pm 0.8) \times 10^{20}$ Mx and $\Phi_\varphi / L \approx (13 \pm 6) \times 10^{20}$ Mx AU^{-1}.

TABLE III

Magnetic fluxes computed for the MC observed on 15 May 1997, at 1 AU.

Model	Φ_z (Mx)	$\Phi_\varphi L^{-1}$ (Mx AU^{-1})
Symmetric model		
Lundquist	5.0×10^{20}	12×10^{20}
Gold–Hoyle	5.1×10^{20}	12×10^{20}
Cid	3.9×10^{20}	13×10^{20}
Mean	4.7×10^{20}	12×10^{20}
S.D.	0.7×10^{20}	0.2×10^{20}
Asymmetric model		
Lundquist (in-bound)	5.7×10^{20}	17×10^{20}
Gold–Hoyle (in-bound)	5.8×10^{20}	17×10^{20}
Cid (in-bound)	4.1×10^{20}	21×10^{20}
Lundquist (out-bound)	4.8×10^{20}	8×10^{20}
Gold–Hoyle (out-bound)	4.9×10^{20}	8×10^{20}
Cid (out-bound)	3.7×10^{20}	5×10^{20}
Mean	4.8×10^{20}	13×10^{20}
S.D.	0.8×10^{20}	6×10^{20}

The first column indicates the models, second and third columns show the values of the axial and azimuthal (per unit length) magnetic fluxes. *First* (*upper*) *block* corresponds to the symmetric fitting, and *second one* (*lower*) to the asymmetric case. *Last two rows* of each block show the means and the standard deviations of the fluxes in each case.

4. Discussion

4.1. Magnetic topology scenario and its link with the interplanetary observations

From our analysis of the magnetic character and evolution of the dimming regions, we propose a scenario which links the formation of the CME with the formation of the coronal dimming regions. We follow the interpretation of Webb *et al.* (2000) that the two main dimming regions of 12 May 1997, do indeed, mark the foot-points of the flux rope that erupts to form the CME.

Kahler and Hudson (2001) state that the contraction of TCHs must be at least partially due to magnetic reconnection. Interestingly, they suggest that larger-scale newly "opened" magnetic field does not re-close in the arcade or even in the vicinity of the neutral line, but with an independent source of "open" magnetic field of opposite polarity. They propose that such a magnetic field could be found in previously existing coronal holes. Combining these ideas with our data analysis suggests the

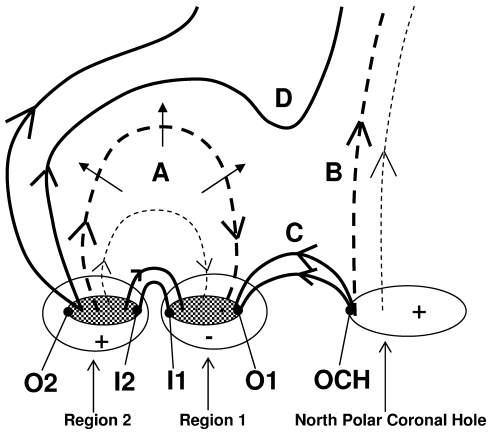

Figure 10. Sketch of the evolution of the global magnetic field topology of the 12 May 1997 CME eruption. *Dashed* (*solid*) *lines* represent the pre (post)-reconnection magnetic structure. The *hashed regions* represent the main dimming regions. **A** and **B** reconnect to form **C** and **D**. **A** marks the expanding magnetic loops connecting the opposite polarity regions in AR8038. **B** marks the positive polarity "open" magnetic field in the north polar coronal hole. **C** marks the reconnected field lines that form between the north polar coronal hole boundary (**OCH**) and the outer boundary of *region* 1 (**O1**). **D** marks the newly "opened" magnetic field. **O1 (I1)** and **O2 (I2)** denote the outer (inner) boundaries of coronal dimming *regions* 1 and 2, respectively.

following scenario (see Figure 10): (**A**) and (**B**) reconnect to form closed loops (**C**) and "open" magnetic field lines (**D**).

The magnetic loops of the CME (**A**) expand and eventually push against the "open" magnetic field lines of the north polar coronal hole (**B**). The polarity of the northern edge of the expanding magnetic loops is negative and the north polar coronal hole field is positive. As the expanding loops push against the oppositely orientated "open" field lines, a current sheet will form at their interface. These represent favourable conditions for successive magnetic reconnection to take place.

After reconnection, magnetic loops (**C**) are created, connecting the positive north polar coronal hole field (**OCH**) with the outer boundary of the negative dimming region 1 (**O1**). These hot loops are actually visible in the SXT image shown in Figure 8, marked by the letter "**C**". This connection acts to close down the outer boundary of the negative dimming region 1, with reconnection of successive field lines closing down the boundary from "outside in". The noticeable shrinking of region 1 at the **O1** boundary (as shown by the contracting contours in Figure 4) starts between 06:49 and 07:34 UT. Likewise, the successive closing down at **OCH** creates a shrinking of the north polar coronal hole boundary (also starting between 06:49 and 07:34 UT), as observed (see Figure 7).

The apparent motion of the polar coronal hole boundary could alternatively be attributed to the influence of loop brightening and 3-D projection effects. However, we argue that such an interpretation is invalid in this case because the polar coronal

boundary remains shrunken, even after the brightening has disappeared (see Figure 7). We are unable to quantitatively assess the influence of 3-D projection effects.

As well as creating closed loops between **O1** and **OCH** as discussed earlier, the magnetic reconnection also creates "open" magnetic field lines (**D**). Upon reconnection with the north polar coronal hole, the magnetic field rooted at **O2** is changed from an expanded loop connectivity to an "open" magnetic field configuration. Successive reconnections, due to the expansion of **A** effectively enforce the effect of an "open" magnetic field at **O2**, maintaining the magnetic field conditions under which plasma evacuation is likely to occur. Our data analysis reflects this: **O2** shows only a reluctant contraction, with successive boundaries rather remaining close to the maximum spatial extent boundary until 09:10 UT (see Figures 4 and 5).

If the flare loops are interpreted as a post-eruptive arcade structure (Carmichael, 1964; Sturrock, 1966; Kopp and Pneuman, 1976), then the inner boundaries (**I1**, **I2**) are probably also closed down due to magnetic reconnection, with the inner boundaries of the dimming regions partially obscured by the bright flare loops.

Concerning the interplanetary observations, when studying the electron distribution function, the presence of counter-streaming electrons in a MC is considered an indication that it is connected to the Sun at both ends (e.g. Richardson *et al.*, 1991; Richardson, 1997; Shodhan *et al.*, 2000). The absence of electron streams is interpreted as a full disconnection; while, when electrons are observed streaming in only one direction, the MC may be connected to the solar surface at one end. This connectivity indicator is applied in general, although intermittency can be present in the electron flux distribution (e.g. Larson *et al.*, 1997). Based on high-energy electron observations, Webb *et al.* (2000) concluded that uni-directional electron flows were present in the MC on 15 May (see their Section 3 and Figure 4, fourth and fifth panels from the bottom). If we compare the cloud orientation and the sense of the axial magnetic field in the MC (Sections 3.1 and 3.2) to the pitch angle distribution of high-energy electrons (mainly Figure 4 in Webb *et al.*, 2000), we can conclude that the end of the MC that could still be connected to the Sun during Wind observations was anchored in a positive polarity region. In view of our new interpretation, we suggest that the location of this anchorage is dimming region 2. Recently, Crooker and Webb (2006) independently suggested a similar scenario.

In summary, expansion of the magnetic field containing the flux rope leads to interaction with the north polar coronal hole magnetic field, which through forced, global-scale interchange reconnection (Crooker, Gosling, and Kahler, 2002) effectively closes part of both dimming region 1 and the north polar coronal hole "open" magnetic field. Thus, dimming region 2, where the magnetic field remains "open", becomes the region where the developing magnetic cloud stays connected to the Sun.

4.2. Quantitative comparison of the dimmings and MC magnetic fluxes

In order to test the validity of our scenario, we compare the magnetic flux in the southern-most dimming region, which as argued earlier, best represents the flux involved in the ejection, with the magnetic flux in the MC. Webb *et al.* (2000) used Lepping *et al.*'s (1990) method to fit the cloud magnetic data to Lundquist's (1950) model. From the derived model parameters, the authors estimated an axial cloud flux of $\approx 7.35 \times 10^{20}$ Mx. This value is three times smaller than the net flux in region 2 (see Table II). When comparing interplanetary to coronal global quantities, it is a common practise to include only the axial cloud flux in the comparison. This is probably because the "standard" view for an ejection is that of an expanding coronal flux tube extending into the interplanetary medium in a self-similar manner. However, in recent works (Mandrini *et al.*, 2005) that quantitatively link interplanetary events to their coronal sources, it was shown that the azimuthal cloud flux should also be included in the comparison. Indeed, when the cloud length can be estimated and the azimuthal flux calculated, it proves to be almost an order of magnitude higher than the axial flux and its value is closer to the solar flux measured in the dimming regions.

As seen in Equation (1), the value of Φ_φ depends on the MC length (L). This parameter is one of the unknowns when modelling a MC magnetic configuration, since *in situ* observations provide data along a single cloud direction. How then, can we estimate a value for L? Because of the presence of unidirectional electron flows, the flux rope was probably attached to the Sun only at one end when observed by Wind. Following our proposed scenario, the disconnection of the ejected rope is related to the reconnection process that shifts the northern coronal hole boundary farther north (see Section 2.7). This process starts at ≈07:00 UT, reaches a maximum at ≈13:00 UT and finishes by ≈19:00 UT on 12 May 1997. We assume that disconnection occurs throughout these 12 h. If we consider the central interval time (13:00 UT) to represent the disconnection time, and taking into account that the MC is observed at Earth 77 h (15 May at ≈10:00 UT) after ejection (on 12 May at ≈05:00 UT), we can estimate a cloud length ≈1.1 AU, neglecting any probable curvature and assuming a constant travel velocity from Sun to Earth. However if, when the flux rope disconnects from the solar surface, it is able to reconnect with the ambient solar wind large-scale field lines, then the magnetic twist contained in the ejected flux tube propagates along the new connections as a torsional Alfvén wave. Taking a typical Alfvén velocity of 100 km s^{-1}, from 13:00 UT, the twist can propagate from the disconnected end of the flux tube over a length of 0.2 AU in the remaining 69 h before the MC arrives at Earth (10:00 UT). Therefore, the probable length of the MC is $L \sim 1.3$ AU, which is a lower limit since, as stated earlier, we are neglecting any flux rope curvature. Finally, the MC fluxes are $\Phi_z \approx (4.8 \pm 0.8) \times 10^{20}$ Mx and $\Phi_\varphi \approx (17 \pm 8) \times 10^{20}$ Mx, with a cloud length of 1.3 AU. This gives the total flux in the MC as $\Phi_{\rm MC} \approx (22 \pm 9) \times 10^{20}$ Mx. We want

to stress that the error bar in the estimated MC flux arises from the fact that the cloud observations are asymmetric, this yields a larger error bar than considering a symmetric model (see Table III).

The value of $\Phi_{MC} \approx (22 \pm 9) \times 10^{20}$ Mx is in very good agreement with the net flux in the southern-most dimming region, $(21 \pm 7) \times 10^{20}$ Mx, that we conclude best represents the cloud flux (see Section 4.1). The measurement of the magnetic flux from dimming region 2 is probably a minimum estimate for the magnetic flux contained within the MC because we are unable to determine the extent to which the dimming regions may extend into the region obscured by the bright flare loops. The flare loops sit at the heart of AR8038 and, therefore, we are potentially failing to measure some contribution of the strong active region solar flux within the dimming regions.

The fact that the azimuthal cloud flux (approximately four times larger than the flux in the axial component) is the closest to the solar flux participating in the ejection should have implications on CME models. In our view, this suggests that during the ejection, twist might be created by reconnection in a sheared arcade overlying the expanding tube, significantly increasing the twist in the ejected flux rope in a similar way as that proposed by Mandrini *et al.* (2005). In such a case, the photospheric "open" flux will mainly contribute to the azimuthal cloud component.

Recently, Odstrcil, Pizzo, and Arge (2005), using a numerical coronal outflow model for this event, found that the excursion of the southern TCH toward the helio-equator was the source of a moderate fast solar wind stream that interacted with the interplanetary CME. In view of our scenario, we propose that the southern TCH was, in fact, where the MC was connected to the Sun. Further, Ivanov *et al.* (2003) concluded that the low-latitude TCH was one of the sources of the near-Earth disturbance, which supports our scenario.

5. Conclusion

Our study uses a specially developed method to quantitatively define coronal dimming region boundaries and to follow their manifestation and evolution. We used SOHO/EIT and MDI and *Yohkoh*/SXT data to analyse the changing intensity and the magnetic character of the coronal dimming regions, as well as the global features that appear in conjunction with the CME eruption from AR8038 on 12 May 1997.

From our analysis of the evolution of the coronal dimming regions and a synthesis of already published results, we derive a new interpretation of this event. We provide multi-wavelength observational evidence to show that the magnetic field of the expanding CME forced global-scale magnetic "interchange reconnection" with "open" field lines of the northern coronal hole, closing down expanding magnetic field lines of the northern side of the CME, while transferring open coronal hole field lines to the southern side. Our scenario explains both the asymmetric temporal

and spatial evolution of the two main dimming regions, as well as the gradual brightening and shrinking of the north polar coronal hole boundary. Combining our scenario with interplanetary observations, we find that the southern-most of the two unidentical twin dimming regions was the principal foot-point of the associated magnetic cloud observed at Earth. This is supported by a thorough analysis of Wind data, using three different magnetic cloud models and two computation methods. We find the magnetic flux from the southern-most dimming region and that of the MC to be in close agreement within the same order of magnitude 10^{21} Mx. This study highlights the crucial contribution of the azimuthal flux in such calculations and has potential implications for CME models.

Acknowledgements

We thank the anonymous referee for helpful comments which greatly improved and clarified this work. SOHO is a project of international cooperation between ESA and NASA. The LASCO CME catalogue is generated and maintained at the CDAW Data Center by NASA and The Catholic University of America in cooperation with the Naval Research Laboratory. This research has made use of NASA's Space Physics Data Facility (SPDF). G.D.R. Attrill is grateful to PPARC for support. M.S.N. is a fellow of CONICET. L.K.H. acknowledges the Leverhulme Trust for the award of a Philip Leverhulme prize. L.v.D.G. acknowledges the Hungarian government grant OTKA 048961. This work was partially supported by the Argentinean grants UBACyT X329, PIP 6220 (CONICET) and PICTs 03-12187 and 03-14163 (ANPCyT). S.D. and C.H.M. are members of the Carrera del Investigador Científico. J.W. acknowledges support from the National Natural Science Foundation of China under the grant 10233050.

References

Berger, T.E. and Lites, B.W.: 2003, *Solar Phys.* **213**, 213.
Bothmer, V. and Schwen, R.: 1998, *Ann. Geophys.* **16**, 1.
Carmichael, H.: 1964, in W.N. Hess (ed.), *AAS-NASA Symposium on Physics of Solar Flares*, NASA-SP 50, p. 451.
Chertok, I.M. and Grechnev, V.V.: 2003, *Astron. Rep.* **47**, 934.
Chertok, I.M. and Grechnev, V.V.: 2005, *Solar Phys.* **229**, 95.
Chertok, I.M., Grechnev, V.V., Hudson, H.S., and Nitta, N.V.: 2004, *J. Geophys. Res.* **109**, 2112.
Cid, C., Hidalgo, M.A., Nieves-Chinchilla, T., Sequeiros, J., and Vinas, A.F.: 2002, *Solar Phys.* **207**, 187.
Crooker, N.U., Gosling, J.T., and Kahler, S.W.: 2002, *J. Geophys. Res.* **107**, 1028.
Crooker, N.U. and Webb, D.F.: 2006, *J. Geophys. Res.* (in press).
de Toma, G., Holzer, T.E., Burkepile, J.T., and Gilbert, H.R.: 2005, *Astrophys. J.* **621**, 1109.
Dasso, S., Mandrini, C.H., Démoulin, P., and Luoni, M.L.: 2006, *Astron. Astrophys.* **455**, 349.

Dasso, S., Mandrini, C.H., Démoulin, P., and Farrugia, C.J.: 2003, *J. Geophys. Res.* **108**, 3.
Dasso, S., Mandrini, C.H., Démoulin, P., Luoni, M.L., and Gulisano, A.M.: 2005, *Adv. Space Res.* **35**, 711.
Delaboudiniére, J.P. *et al.*: 1995, *Solar Phys.* **162**, 291.
Gold, T. and Hoyle, F.: 1960, *Monthly Notices Roy. Astron. Soc.* **120**, 89.
Green, L.M., Démoulin, P., Mandrini, C.H., and van Driel-Gesztelyi, L.: 2003, *Solar Phys.* **215**, 307.
Hagenaar, H.J., Schrijver, C.J., and Title, A.M.: 2003, *Astrophys. J.* **584**, 1107.
Hansen, R.T., Garcia, C.J., Hansen, S.F., and Yasukawa, E.: 1974, *Publ. Astron. Soc. Pacific* **86**, 500.
Harra, L.K. and Sterling, A.C.: 2001, *Astrophys. J.* **561**, L215.
Harrison, R.A. and Lyons, M.: 2000, *Astron. Astrophys.* **358**, 1097.
Hudson, H.S., Acton, L.W., and Freeland, S.L.: 1996, *Astrophys. J.* **470**, 629.
Ivanov, K.G., Belov, A.V., Kharshiladze, A.F., Romashets, E.P., Bothmer, V., Cargill, P.J., and Veselovsky, I.S.: 2003, *Int. J. Geomagn. Aeron.* **4**, 91.
Kahler, S.W. and Hudson, H.S.: 2001, *J. Geophys. Res.* **106**, 29239.
Kopp, R.A. and Pneuman, G.W.: 1976, *Solar Phys.* **50**, 85.
Larson, D.E. *et al.*: 1997, *Geophys. Res. Lett.* **24**, 1911.
Lepping, R.P. *et al.*: 1995, *Space Sci. Rev.* **71**, 207.
Lundquist, S.: 1950, *Ark. Fys.* **2**, 361.
Mandrini, C.H. *et al.*: 2005, *Astron. Astrophys.* **434**, 725.
Odstrcil, D., Pizzo, V.J., and Arge, C.N.: 2005, *J. Geophys. Res.* **110**, 2106.
Podladchikova, O. and Berghmans, D.: 2005, *Solar Phys.* **228**, 265.
Richardson, I.G., Farrugia, C.J., and Burlaga, L.F.: 1991, in *Proceedings of the 22nd International Cosmic Ray Conference*, NASA A92-36806 15-93, p. 9.
Richardson, I.G.: 1997, in N. Crooker, J.A. Jocelyn and J. Feynman (eds.), *Coronal Mass Ejections, Geophysical Monograph 99*, American Geophysical Union, Washington DC, p. 189.
Rust, D.M.: 1983, *Space Sci. Rev.* **34**, 21.
Scherrer, P.H. *et al.*: 2005, *Solar Phys.* **162**, 129.
Shodhan, S. *et al.*: 2000, *J. Geophys. Res.* **105**, 27261.
Sonnerup, B.U.Ö. and Scheible, M.: 1998, *ISSI Science Report*, SR-001, Kluwer Academic Publishers, Dordrecht.
Sterling, A.C. and Hudson, H.S.: 1997, *Astrophys. J.* **491**, L55.
Sterling, A.C. and Moore, R.L.: 2001, *J. Geophys. Res.* **106**, 25227.
Sturrock, P.A.: 1966, *Nature* **211**, 695.
Thompson, B.J., Cliver, E.W., Nitta, N., Delannée, C., and Delaboudinière, J.P.: 2000, *Geophys. Res. Lett.* **27**, 1431.
Thompson, B.J., Plunkett, S.P., Gurman, J.B., Newmark, J.S., St. Cyr, O.C., and Michels, D.J.: 1998, *Geophys. Res. Lett.* **25**, 2461.
Tsuneta, S. *et al.*: 1991, *Solar Phys.* **136**, 37.
Wang, J., Zhou, G., Wang, Y., and Song, L.: 2003, *Solar Phys.* **216**, 143.
Wang, T., Yan, Y., Wang, J., Kurokawa, H., and Shibata, K.: 2002, *Astrophys. J.* **572**, 580.
Webb, D.F. *et al.*: 2000, *J. Geophys. Res.* **105**, 27251.
Zarro, D.M., Sterling, A.C., Thompson, B.J., Hudson, H.S., and Nitta, N.: 1999, *Astrophys. J.* **520**, L139.
Zhukov, A.N. and Auchère, F.: 2004, *Astron. Astrophys.* **427**, 705.